



## RESEARCH ARTICLE

10.1029/2021MS002844

This article is a companion to Stanley et al. (2020), <https://doi.org/10.1029/2020MS002185>.

## Key Points:

- Coarse-resolution ocean model density fields contain systematic errors due to subgrid-scale variance
- Parameterizations of density correction cause circulation changes in the North and South Atlantic Ocean
- Parameterizations reduce coarse-resolution model biases in the Gulf Stream representation

## Supporting Information:

Supporting Information may be found in the online version of this article.

## Correspondence to:

I. Grooms,  
[ian.grooms@colorado.edu](mailto:ian.grooms@colorado.edu)

## Citation:

Kenigson, J. S., Adcroft, A., Bachman, S. D., Castruccio, F., Grooms, I., Pegion, P., & Stanley, Z. (2022). Parameterizing the impact of unresolved temperature variability on the large-scale density field: 2. Modeling. *Journal of Advances in Modeling Earth Systems*, 14, e2021MS002844. <https://doi.org/10.1029/2021MS002844>

Received 24 SEP 2021  
Accepted 10 FEB 2022

# Parameterizing the Impact of Unresolved Temperature Variability on the Large-Scale Density Field: 2. Modeling

J. S. Kenigson<sup>1</sup> , A. Adcroft<sup>2,3</sup> , S. D. Bachman<sup>4</sup> , F. Castruccio<sup>4</sup> , I. Grooms<sup>1</sup> , P. Pegion<sup>5</sup>, and Z. Stanley<sup>5,6</sup> 

<sup>1</sup>Department of Applied Mathematics, University of Colorado Boulder, Boulder, CO, USA, <sup>2</sup>Geophysical Fluid Dynamics Laboratory, National Oceanic and Atmospheric Administration, Princeton, NJ, USA, <sup>3</sup>Atmospheric and Oceanic Sciences, Princeton University, Princeton, NJ, USA, <sup>4</sup>Climate and Global Dynamics Laboratory, National Center for Atmospheric Research, Boulder, CO, USA, <sup>5</sup>NOAA Physical Sciences Laboratory, Boulder, CO, USA, <sup>6</sup>Cooperative Institute for Research in Environmental Sciences, University of Colorado, Boulder, CO, USA

**Abstract** Ocean circulation models have systematic errors in large-scale horizontal density gradients due to estimating the grid-cell-mean density by applying the nonlinear seawater equation of state to the grid-cell-mean water properties. In frontal regions where unresolved subgrid-scale (SGS) fluctuations are significant, dynamically relevant errors in the representation of current systems can result. A previous study developed a novel and computationally efficient parameterization of the unresolved SGS temperature variance and resulting density correction. This parameterization was empirically validated but not tested in an ocean model. In this study, we implement deterministic and stochastic variants of this parameterization in the pressure-gradient force term of a coupled ocean-sea ice configuration of the community Earth system model-modular ocean model version 6 and perform a suite of hindcast sensitivity experiments to investigate the ocean response. The parameterization leads to coherent changes in the large-scale ocean circulation and hydrography, particularly in the Nordic Seas and Labrador Sea, which are attributable in large part to changes in the seasonally varying upper-ocean exchange through Denmark Strait. In addition, the separated Gulf Stream strengthens and shifts equatorward, reducing a common bias in coarse-resolution ocean models. The ocean response to the deterministic and stochastic variants of the parameterization is qualitatively, albeit not quantitatively, similar, yet qualitative differences are found in various regions.

**Plain Language Summary** In ocean models, the location and strength of current systems are related to horizontal gradients of the seawater density. The density of seawater is calculated using an equation of state which depends on the temperature and salinity. These water properties could vary considerably over the spatial scale of one model grid box, yet ocean models resolve only grid-cell-mean water properties. As the seawater equation of state is nonlinear, density gradients which are calculated by applying this equation to the grid-cell-mean water properties could contain errors which result in the misrepresentation of current systems. Therefore, parameterizations have been developed to represent the unknown subgrid-scale water property variance in terms of resolved variables, allowing for a correction to the resolved density field. In this study, we implement and test a parameterized density correction in a coupled ocean-sea ice configuration of the community Earth system model-modular ocean model version 6. The ocean response to the density correction consists of large-scale circulation changes, particularly in the Atlantic Ocean. The representation of the Gulf Stream, a dynamically important current for the global ocean circulation, is found to improve.

## 1. Introduction

The horizontal resolution of ocean circulation models remains limited by computational constraints, particularly in global-scale climate simulations. Coarse-resolution ocean models, with a representative grid-cell size of  $\sim 1^\circ$ , generally do not resolve mesoscale and submesoscale variability. Yet such variability makes critical contributions to the ocean circulation and heat transport, and parameterizations are commonly used to represent unresolved subgrid-scale (SGS) processes in terms of resolved variables. Recently, it has been appreciated that unresolved SGS water property variability, associated both with eddies and the mean state, introduces uncertainties and errors into the large-scale density field. These errors, in turn, can result in the misrepresentation of the buoyancy force and thus the hydrostatic pressure gradient. Uncertainties in horizontal pressure gradients are a consequence of the nonlinearity of the seawater equation of state (EOS), which evaluates density as one of several empirically

derived functions of temperature, salinity, and pressure. Such equations are valid for a water parcel in thermodynamic equilibrium. Yet coarse-resolution ocean general circulation models calculate the grid-cell-mean density by applying the EOS to the grid-cell-mean water properties, an approximation which introduces dynamically relevant errors in frontal regions where unresolved SGS variability can be significant (Brankart, 2013).

To account for these errors, Brankart (2013) implemented a stochastic parameterization of the corrected density in the pressure gradient force (PGF) of the horizontal momentum equation in a coarse-resolution ( $\sim 2^\circ$ ), stand-alone configuration of NEMO (ORCA2). Specifically, a corrected density was calculated as a mean of densities obtained by applying the seawater EOS to the grid-cell-mean temperature and salinity, perturbed via  $p$  local random walks, where  $p$  is a model parameter. In one sensitivity experiment, this parameterization reduced biases in the mean state which are widely observed in coarse-resolution ocean models, such as in the Gulf Stream separation and transport, air-sea heat fluxes in the North Atlantic Ocean, and the sea surface height (SSH) gradient between the tropical Atlantic and Pacific Oceans. Furthermore, in an eddy-resolving ( $\sim 0.25^\circ$ ) configuration of NEMO (NATL025), the stochastic density correction of Brankart (2013) improved the Gulf Stream representation (Zanna et al., 2019). Using a different approach, Williams et al. (2016) implemented a stochastic perturbation of the temperature tendency in a coarse-resolution ( $\sim 2.5 \times 3.75$ ) configuration of the FAMOUS ocean-atmosphere general circulation model, which reduced biases in the sea surface temperature and salinity.

However, the relationship between the Brankart (2013) density parameterization and the true mean density has not been validated quantitatively. For this reason, Stanley et al. (2020) derived a mathematical relationship between the true mean density and the unresolved SGS temperature variability. (The contribution from the unresolved SGS salinity variability was found to be negligible; see also Williams et al. (2016)). Using this relationship, they developed two versions of a SGS temperature variance parameterization which takes into account the spatial and temporal structure as diagnosed from an eddy-resolving ( $\sim 0.1^\circ$ ) configuration of the POP model. One parameterization is deterministic, expressing the SGS temperature variance in terms of horizontal gradients of the resolved temperature field. The stochastic variant conceptualizes individual realizations of SGS turbulence as fundamentally random, thus representing spread about the deterministic model; in particular, the stochastic parameterization replaces the fixed amplitude of the deterministic parameterization with a log-normally distributed random process. Both versions of the SGS temperature variance parameterization have been shown to demonstrate high goodness-of-fit to that diagnosed from the eddy-resolving simulation (Stanley et al., 2020). However, the parameterization has not previously been implemented in an ocean model, and the ocean response to the density corrections remains unknown. Furthermore, as the Brankart (2013) study tested a stochastic parameterization exclusively, the attribution of the mean ocean response to the mean of the parameterization versus the rectified effects of the noise was not possible.

In this study, we perform a suite of sensitivity experiments to investigate the dynamical effects of the Stanley et al. (2020) parameterizations in a coarse-resolution ( $\sim 0.66^\circ$ ) configuration of the Modular Ocean Model version 6 (MOM6). The parallel use of deterministic and stochastic versions of the SGS temperature variance parameterization permits the attribution of the mean ocean response to mean density correction versus noise. Section 2 describes the model configuration and provides a detailed summary of the experimental protocol. Section 3 examines the effects of the parameterizations, both globally and in selected dynamically relevant current systems. Finally, Section 4 summarizes this study, compares the results with prior stochastic modeling studies, and states the conclusions.

## 2. Methods

MOM6 solves the hydrostatic primitive equations on an Arawaka C-grid and features several advancements over its predecessors, including the use of vertical Lagrangian discretization with remapping to permit arbitrary vertical coordinates (Adcroft et al., 2019). MOM6 was coupled to the Los Alamos Sea Ice Model (CICE version 5 Hunke et al., 2010) in the framework of the Community Earth System Model (CESM) version 2.2 (Danabasoglu et al., 2020). The CESM-MOM6 model was configured as a coupled ocean-sea ice model forced at the surface with historical atmospheric state and flux fields provided by the Japanese 55-year atmospheric reanalysis product (JRA55-do; Tsujino et al. (2018)). The model has a nominal spatial resolution of  $\sim 0.66^\circ$  and 65 vertical layers in  $z^*$  coordinates with depths ranging from  $\sim 1.25$ – $5,876$  m; The layer spacing varies and is refined in the upper ocean (see the description of  $z^*$  coordinates in Adcroft and Campin (2004)). The GEOMETRIC parameterization

of Marshall et al. (2012) was used to represent the extraction of available potential energy from the mean flow by mesoscale eddies within the Gent-McWilliams (1990) framework. Vertical mixing in the turbulent boundary layer is represented using the K-Profile Parameterization (KPP) of Large et al. (1994), implemented via the CVMix package. MOM6 was configured to use the Wright seawater EOS (Wright, 1997). At the time the simulations described herein were performed, the model parameters were chosen for consistency with one of several “best” configurations of MOM6 within the CESM 2.2 framework, although MOM6 configurations remain under development within this framework and model tuning is ongoing.

The density corrections resulting from the SGS temperature variance parameterizations of Stanley et al. (2020) were implemented in the PGF. Specifically, Stanley et al. (2020) used a Taylor expansion to relate the mean density to the unresolved SGS temperature variance:

$$\bar{\rho} \approx \hat{\rho}(\bar{T}, \bar{S}) + \frac{\partial^2 \hat{\rho}(\bar{T}, \bar{S})}{2} \sigma_T^2. \quad (1)$$

Here  $\bar{\rho}$  is the true grid-cell-mean density;  $\hat{\rho}$  is the seawater EOS (dependence on pressure has been omitted to condense notation);  $\bar{T}, \bar{S}$  are the grid-cell-mean temperature and salinity; and  $\sigma_T^2$  is the unresolved SGS temperature variance.

In the deterministic parameterization, the SGS temperature variance is expressed in terms of finite differences of the resolved temperature field. In particular,

$$\sigma_T^2 \approx c \left| \delta x \circ \nabla \bar{T} \right|^2, \quad (2)$$

where  $\delta x$  is the horizontal grid cell size,  $c$  is a parameter to be tuned, and  $\circ$  is the Hadamard product. In the stochastic parameterization, the amplitude of  $\sigma_T^2$  is scaled by a lognormally distributed random variable  $e^\chi$ ; here  $\chi$  is a Gaussian random field with zero mean and constant variance  $\sigma_\chi^2$ :

$$\sigma_T^2 \approx c e^\chi \left| \delta x \circ \nabla \bar{T} \right|^2. \quad (3)$$

(Therefore, the medians of the deterministic and stochastic parameterizations are equal, while the mean of the stochastic parameterization is 21.5% greater than the mean of the deterministic parameterization, as discussed in Stanley et al. (2020).) Here  $\chi$  is uncorrelated in space and has an AR (1) structure in time:

$$\chi(x, y, t) = \phi(x, y, t) \chi(x, y, t - \delta t) + \epsilon(x, y, t), \quad (4)$$

where  $\epsilon$  is a Gaussian random field with zero mean and no correlations in horizontal space  $(x, y)$  or time  $(t)$ . The variance of the noise  $\epsilon$  varies with the AR (1) parameter  $\phi$  so as to keep the process variance  $\sigma_\chi^2$  constant; Stanley et al. (2020) diagnosed  $\sigma_\chi^2 \approx 0.39$  from a high-resolution POP simulation (see Equation 44 of that study and surrounding discussion). Here  $\phi$  is related to a decorrelation timescale  $\tau$  via

$$\phi(x, y, t) = e^{-\delta t / \tau(x, y, t)}, \quad (5)$$

where  $\delta t = 1,800$  s is the model baroclinic timestep, and

$$\tau = k \sqrt{\frac{u^2(x, y, t) + v^2(x, y, t)}{\delta x^2 + \delta y^2}}. \quad (6)$$

Here  $(u, v)$  represent the instantaneous velocity of the upper-most layer. Stanley et al. (2020) diagnosed the scaling factor  $k = 3.7$  from the same high-resolution simulation described previously, and our study retains this choice. For the spatial variability of the diagnosed and modeled decorrelation timescale, the reader is referred to Figure 6 therein.

The amplitude of the density corrections is determined by the scaling factor  $c$  in Equation 2. While Stanley et al. (2020) developed heuristics for choosing the magnitude of this constant based on the horizontal grid-cell size, it is expected that the optimal value of  $c$  is a model- and physics-dependent quantity. In addition, Stanley et al. (2020) estimated optimal choices of  $c$  as a function of grid-cell resolution by coarse-graining temperature

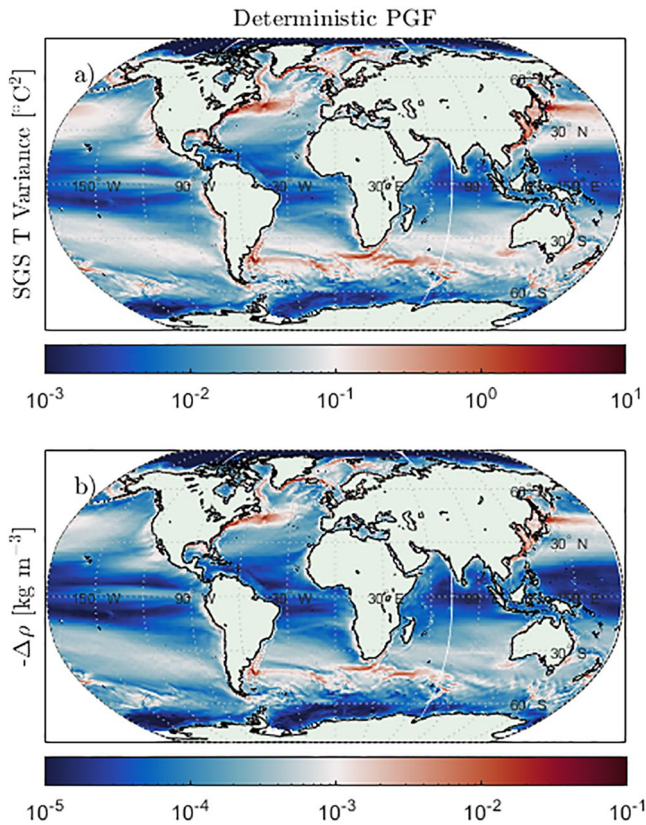


**Figure 1.** (a) Parameterized subgrid-scale (SGS) temperature variance in the deterministic pressure gradient force Run. (b)  $-\Delta\rho$ , the negative of the density correction from Equation 1 corresponding to the SGS temperature variance parameterization in panel (a); note the use of logarithmic scales. Data are 50-year means at a depth of 2.5 m.

data (referenced to an eddy-resolving, nominally  $0.1^\circ$  POP grid) offline. Some heuristics for the choice of  $c$  are provided in Figure A1 of that study. This analysis suggests a prior choice of  $c \approx 0.2$  for a  $\sim 1^\circ$  model. However, the temperature gradient in a coarse-resolution model is generally weaker than that obtained by coarse-graining the temperature field of a high-resolution model. In this study, we therefore expected a priori to require a larger value of  $c$  and performed only preliminary tuning, given that MOM6 is under active development in CESM and tuning of parameters in the base case is currently ongoing. In particular, a factor of  $c = 0.5$  was selected for the Experimental Runs. The scheme was effectively disabled along boundaries, as the representation of layers in shallow regions in this configuration of MOM6 posed numerical difficulties, and Stanley et al. (2020) had not validated the parameterization there.

All runs were initialized from the ocean/sea ice state that resulted from a prior simulation forced with 58 years of the JRA55-do historical atmospheric variables (Tsujino et al., 2018). A Control Run, in which the SGS temperature variance parameterization was disabled, was then integrated for 1 year (to complete the sequence of 59 years of available JRA55-do v1.3, historically varying forcing fields), and then for an additional 59 years, that is, for the period of 1,958–2016. Next, two Experimental Runs were performed in which either the deterministic or stochastic version of the parameterization was enabled in the PGF (hereafter referred to as Deterministic PGF Run and Stochastic PGF Run, respectively). Other model parameters were chosen for consistency with the prior run.

MOM6 was configured to output monthly mean data which was remapped vertically from its native 65 layers in  $z^*$ -coordinates to a set of 34 standard levels from the WOA09 (Griffies et al., 2020; White et al., 2009). To represent the ocean long-term mean state, the initial 9 years of the simulation were disregarded as a spinup and the final 50 years were averaged in time; monthly and seasonal climatologies were formed for the same period. To represent the variability, variances on timescales ranging from twice the thermodynamic timestep ( $dt = 3,600$  s) to 50 years were calculated. Although the model was

configured to output monthly mean data, it was possible to compute variance on shorter time scales than monthly by configuring the model to output monthly means of the square of the water properties. Variance was then subsequently computed as the mean of the square minus the square of the mean.

Hereafter, the ocean response to the density corrections will be assessed by considering anomalies of the long-term mean state and variability in the Experimental Runs relative to the Control Run. Subsequent analysis will focus upon changes in the ocean circulation in the range of  $\sim 0$ –400 m, as lateral temperature gradients and hence the SGS temperature variance parameterizations are expected to be greatest near the surface based on the results of Stanley et al. (2020). The spatial pattern of the SGS temperature variance parameterization (Figure 1a) and that of the associated density corrections (Figure 1b) in MOM6 are generally consistent with that of Stanley et al. (2020); the parameterization has the greatest amplitude in frontal regions with large lateral temperature gradients.

### 3. Ocean Dynamical Response to the Density Corrections

#### 3.1. Summary of Ocean Response

The ocean mean state of temperature and salinity, at 200 m, and SSH as simulated in the Control Run are shown in Figures 2a–2c (for completeness, we also show fields at depths 2.5 m, 100 and 400 m in S1–S3a and S3b in Supporting Information S1). Here the SSH field represents dynamic sea level with a correction for the sea ice inverse barometer effect and zero global area mean (Griffies et al., 2016). In the range of  $\sim 0$ –400 m, the SSH and water property changes in the Experimental Runs relative to the Control Run are most pronounced near the Gulf



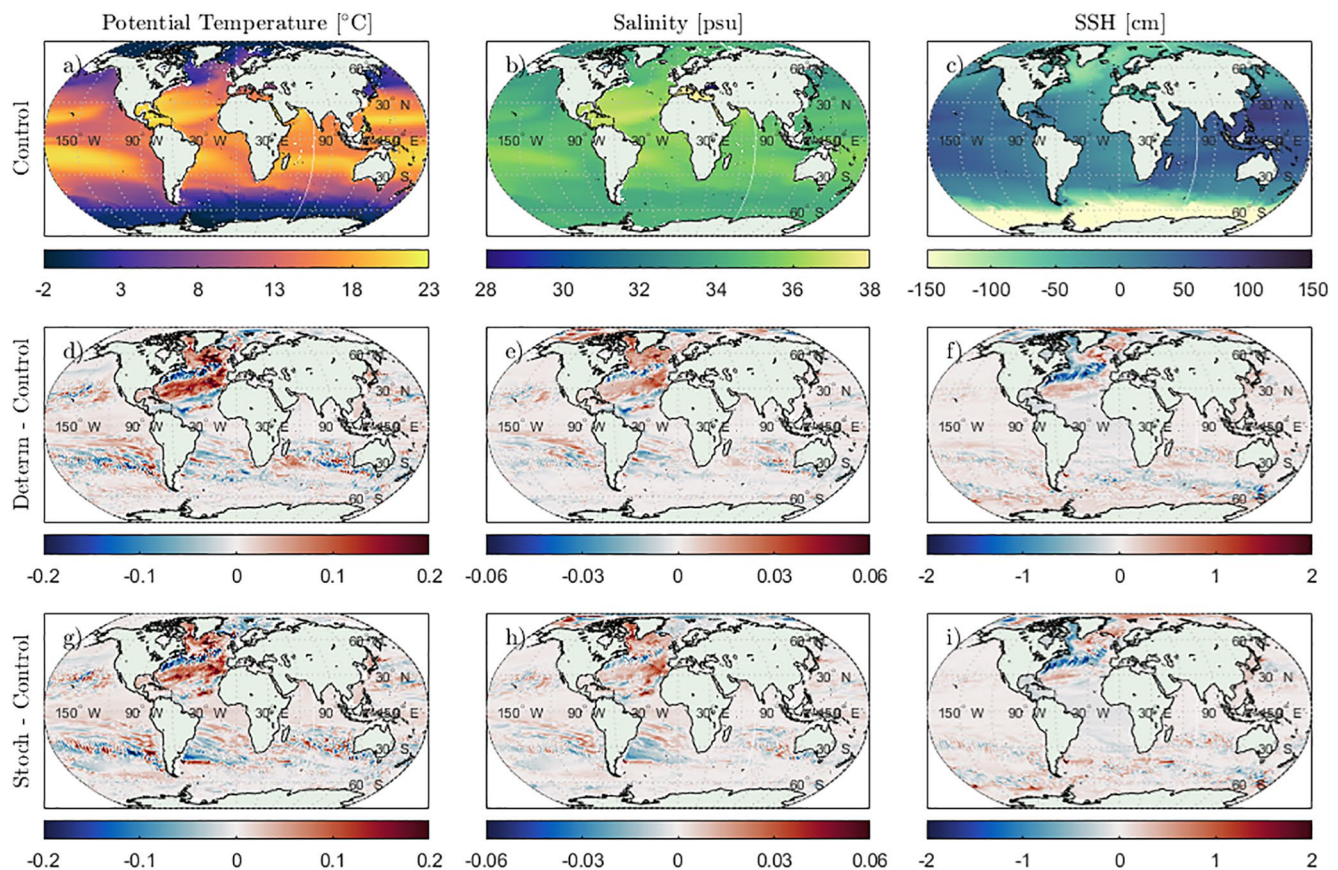


**Figure 2.** (a–c) Control run 50-year-mean state of (a) potential temperature at 200 m, (b) salinity at 200 m, (c) sea surface height. (d–f) Deterministic pressure gradient force (PGF) Run minus Control Run of indicated variable. (g–i) Same as (d–f), but for Stochastic PGF Run minus Control Run.

Stream and North Atlantic Current, the Kuroshio Current, the Agulhas Current, and the Brazil-Malvinas Confluence region (Figures 2d–2i, S1, S2 and S3c–S3f in Supporting Information S1). Near the Gulf Stream, the circulation change is indicated by a dipole pattern in the SSH field (Figures 2f and 2i) the cause of which is discussed in Section 3.3. The upper-ocean temperature and salinity along the path of the separated Gulf Stream and North Atlantic Current are observed to decrease in the Experimental Runs relative to the Control Run (Figures 2d, 2e, 2g and 2h, S1, S2 and S3c–S3f in Supporting Information S1). On the other hand, along the southern flank of the Gulf Stream and in the subtropical gyre, the upper-ocean temperature and salinity increase. The Nordic Seas are cooler and fresher, while the Labrador Sea is warmer and saltier, in the Experimental Runs than in the Control Run (Figures 2d, 2e, 2g and 2h, S1, S2 and S3c–S3f in Supporting Information S1). Associated with these changes, the SSH generally increases in the Nordic Seas and decreases in the Labrador Sea (Figures 2f and 2i). Section 3.2 investigates the physical mechanisms which account for the circulation and hydrographic changes in the subpolar North Atlantic Ocean. Finally, in the South Atlantic Ocean, circulation changes near the Brazil-Malvinas Confluence are evidenced by the water property anomalies (relative to the Control Run) and SSH dipole there; these signals are predominantly seen in the Stochastic PGF Run, and are weak or absent in the Deterministic PGF Run (Figures 2d–2i, S1, S2 and S3c–S3f in Supporting Information S1). The ocean dynamical response in the South Atlantic Ocean is the focus of Section 3.4.

In general, the spatial pattern of the upper-ocean response is qualitatively similar in the Deterministic PGF Run and Stochastic PGF Runs, although differences can be observed, such as near the Brazil-Malvinas Confluence (Figures 2d–2i, S1–S3c–f in Supporting Information S1). In many regions, the amplitude of the response is greater in the Stochastic PGF Run than in the Deterministic PGF Run, yet some exceptions exist; specific regional characteristics of the differences will be investigated in Sections 3.2, 3.3, and 3.4. These findings suggest that the majority of the mean ocean response is associated with the mean density correction, while the rectified effects of the noise play a lesser, albeit non-negligible, role.

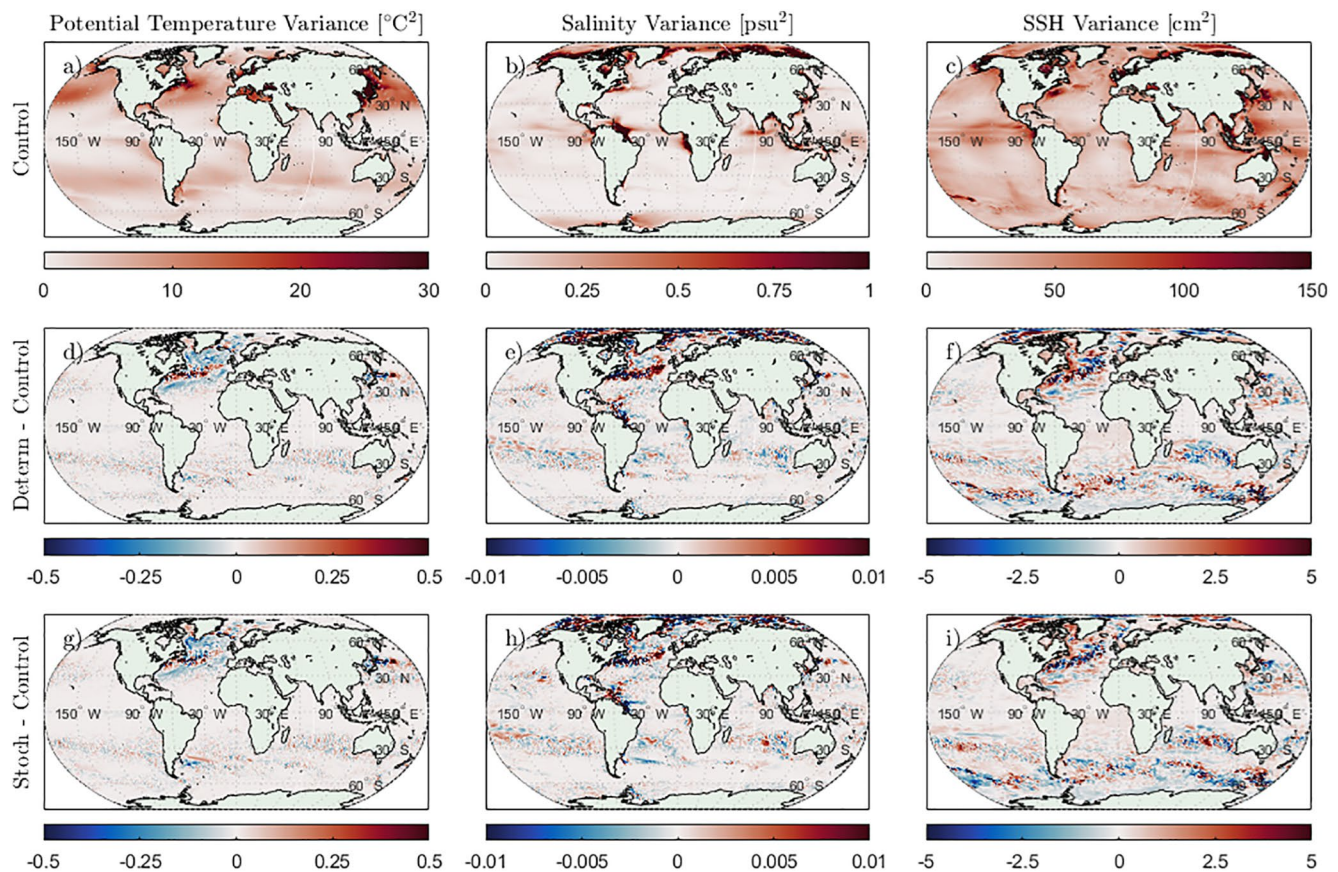


**Figure 3.** (a–c) Control Run variance of (a) potential temperature at 2.5 m, (b) salinity at 2.5 m, (c) sea surface height. (d–f) Deterministic pressure gradient force (PGF) Run minus Control Run of indicated variable. (g–i) Same as (d–f), but for stochastic PGF Run. The timescales represented range from 2 hr to 50 years.

The Control Run variance of temperature, salinity (at 2.5 m), and SSH are shown in Figures 3a–3c. Overall, the changes in water property and SSH variance in the Experimental Runs relative to the Control Run are modest (Figures 3d–3i). Despite the introduction of random noise into the SGS temperature variance parameterization in the Stochastic PGF Run, the differences in variance relative to the Control Run are similar to those of the Deterministic PGF Run (Figures 3d–3i). Notably, the parameterized density corrections reduce the SSH and/or water property variance in certain regions of the separated Gulf Stream, Labrador Sea, and Irminger Sea. In the subpolar gyre of the North Atlantic Ocean, the reduced variance in the 2.5-m temperature may be related to the deepening of wintertime mixed-layer depths (MLDs), as a homogenization of water properties over a greater depth of the water column would be expected to result in reduced variability due to surface forcing and entrainment; however, this remains uncertain. The Gulf Stream region will be explored in greater detail in Section 3.3.

The stochastic perturbations introduced to the density by the parameterization are uncorrelated in space. The lateral gradient of these perturbations appears in the momentum equations, which implies that the noise forcing is concentrated at the smallest scales that can be represented on the grid; in a spatially homogeneous setting the spectrum of the noise forcing in the momentum equation would be proportional to  $k^{-3}$  where  $k$  is the magnitude of the spatial wavenumber. This is also the spectrum associated with backscatter due to Reynolds stresses in quasigeostrophic turbulence (Grooms et al., 2015). Grooms et al. (2015) found that the combination of viscous closures and low-order discretizations combine to prevent noise forcing concentrated at the smallest scales of a parameterized model from cascading back up to large scales; the same mechanism is presumably at play here, damping the ability of the model to respond to the stochastic forcing with increased variability at large scales and long times. This is exacerbated by the fact that backscatter associated with Reynolds stresses (as studied by Grooms et al. (2015)) occurs wherever the eddy kinetic energy is large, whereas the backscatter associated with density corrections is confined to a smaller subset of the domain where there are large resolved temperature gradients. Some combination of Reynolds-stress-driven backscatter (e.g., Bachman, 2019; Jansen et al., 2019;



Juricke et al., 2020), backscatter associated with density corrections, and other forms of stochastic noise (e.g., Grooms, 2016; Grooms & Kleiber, 2019) may be necessary to achieve a large increase in low-resolution model variability.

### 3.2. Nordic Seas and Labrador Sea

The Nordic Seas are a region at the interface of the Arctic Ocean and North Atlantic Ocean, and the hydrographic conditions reflect the exchange of water masses with both sources. Along with the Labrador Sea, the Nordic Seas are a principal site of deep convective mixing in the North Atlantic Ocean, a process which takes place when strong air-sea heat fluxes cause upper-ocean buoyancy loss and destabilize the stratification. In the Control Run, deep convection takes place within the Nordic Seas, Labrador Sea, Irminger Sea, and in other localized regions (Figure 5a). Ocean modeling studies have linked wintertime deep convection in these regions with the strength of the Atlantic Meridional Overturning Circulation (Heuzé, 2017), which has wide-reaching interconnections with the global ocean circulation. Given the importance of these regions for the accurate representation of the ocean circulation, we summarize the ocean general circulation pathways and hydrographic conditions here.

Along the western boundary of the Nordic Seas, the East Greenland Current transports relatively cold, fresh water south from the Arctic Ocean through the Nordic Seas via Fram Strait. The East Greenland Current flows southward along the coast of Greenland through Denmark Strait, continuing west of Cape Farewell as the West Greenland Current, and forming the northern flank of the subpolar gyre in the North Atlantic Ocean. A branch of the East Greenland Current, the East Icelandic Current, bifurcates from the East Greenland Current north of Denmark Strait and flows eastward to the north of Iceland. At the same time, the Irminger Current, as well as its extension, the North Icelandic Irminger Current, transport relatively warm, saline Atlantic water northward via the eastern Denmark Strait and then eastward around Iceland into the Nordic Seas. Additional branches of the North Atlantic Current enter the Nordic Seas across the Greenland-Scotland Ridge, and warm, saline currents flow northward along the eastern boundary of the Nordic Seas before partially recirculating south of Fram Strait. The Nordic Seas circulation and hydrographic conditions are detailed by Latarius and Quadfasel (2016); see their Figure 1. The Polar Front represents the boundary between the Arctic-origin inflow in the East Greenland Current and the Nordic Seas interior and is present in the Control Run as a region of strong lateral temperature and salinity gradients (Figures 4a and 4b, other depths shown in S4, S5, S6a and S6b in Supporting Information S1). In the Control Run, sea ice is present in winter near the cold, fresh boundary currents of the Nordic Seas and subpolar gyre (Figure 5b).

The ocean response to the density corrections in the near-surface (i.e., 2.5 m) is characterized by cooling and freshening in the Nordic Seas and warming and salinification in the Labrador Sea (here we focus particularly on wintertime conditions; Figures 4c–4f). In the upper ocean, this signal generally attenuates with depth, and in certain regions reverses, by 400 m (Figures 4c–4f, S4, S5, and S6c–S6f in Supporting Information S1). Within the Nordic Seas, the Iceland Sea is the epicenter of the near-surface changes in the ocean mean state, which locally reach  $\sim 0.5^{\circ}\text{C}$  and  $\sim 0.1$  psu or more in the Stochastic PGF Run. Consistent with these hydrographic changes, a band of increased sea ice area (not shown) and thickness (Figures 5d–5f) is present in the western Nordic Seas; in contrast, the sea ice cover is reduced along the Labrador Current. The responses are similar in the Stochastic PGF Run and Deterministic PGF Run, although the amplitude of the changes is generally greater in the Stochastic PGF Run (Figures 4, 5g–5h, S4, S5, S6g and S6h in Supporting Information S1). However, exceptions exist, as can be seen, for example, from the changes in the potential temperature and sea ice fields in the western Nordic Seas at 2.5 m (Figures 4, 5g–5h).

Changes in the ocean circulation and exchange between the Nordic Seas and subpolar North Atlantic Ocean are implicated in the hydrographic changes in the Nordic Seas and Labrador Sea in the Experimental Runs relative to the Control Run. Associated with the lateral temperature gradients near the East Greenland Current, the SGS temperature variance and density parameterizations are highly active (Figures 1a and 1b), and near the surface, there is considerable seasonal variability of the position and strength of maximum temperature gradients (Figure S7a–S7d in Supporting Information S1). In the Control Run, the simulated exchange exhibits seasonal variability, and the East Greenland Current outflow is weakest in summer (JAS; Figures 6a–6d). The density corrections modify the PGF near the East Greenland Current north of Denmark Strait, leading to a reduction in the upper-ocean exchange through Denmark Strait. In particular, there is a decrease in the southward transport of cold, fresh water and northward transport of warm, saline water in the core of the simulated East Greenland

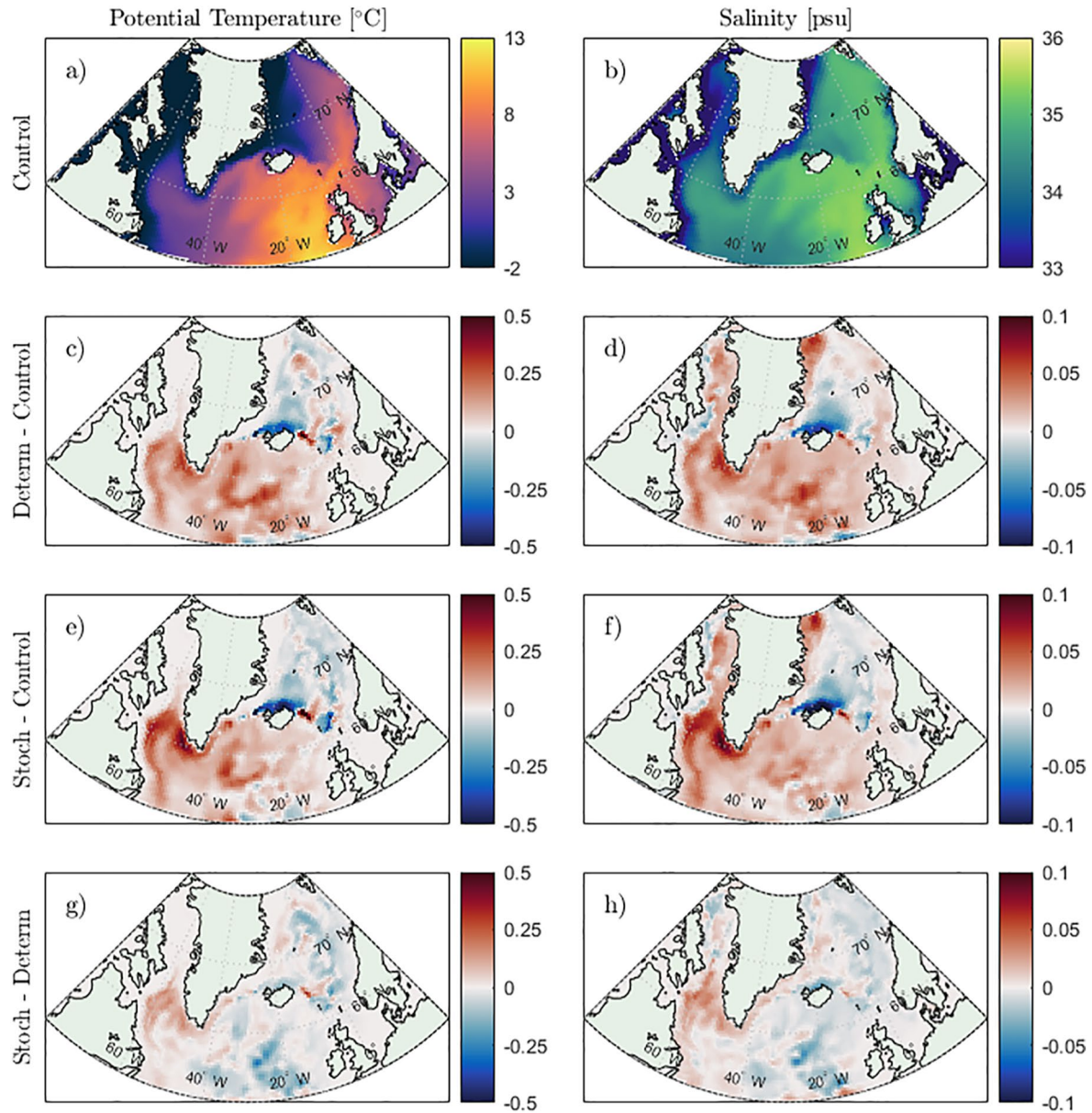


**Figure 4.** (a–b) Control Run 50-year wintertime (JFM) mean state of (a) potential temperature at 2.5 m, and (b) salinity at 2.5 m. (c–d) Deterministic pressure gradient force (PGF) Run minus Control Run of indicated variable. (e–f) stochastic PGF Run minus Control Run of indicated variable. (g–h) stochastic PGF Run minus deterministic PGF Run of indicated variable.

Current and North Icelandic Irminger Currents, that is, above  $\sim 200$  m (Figures 6e–6h). The use of the corrected density reduces the exchange throughout the year, although the absolute change is greatest during the summer (Figure 6e). The circulation changes are associated with a dipole in upper-ocean temperature and salinity anomalies (relative to the Control Run) which develops northwest of Iceland in summer (Figure 7a). The negative temperature and salinity anomaly circulates into the Nordic Seas north of Iceland and follows cyclonic circulation pathways through the Nordic Seas interior, resulting in cooling and freshening relative to the Control Run (Figures 7a–7d). The positive temperature and salinity anomaly is exported in the East Greenland Current, as indicated by the band of relatively warm and saline water along the Greenland shelf between Iceland and Cape Farewell in autumn (Figure 7b). The warm and saline signal is present in the West Greenland Current and Labrador Current by winter and is amplified (Figure 7c). Qualitatively similar responses are found in the Deterministic PGF Run as in the Stochastic PGF Run, albeit with a reduced amplitude (Figures 4g–4h, S4, S5, S6g and S6h in Supporting Information S1; also compare Figures 7a–7d and S8a–S8d in Supporting Information S1).



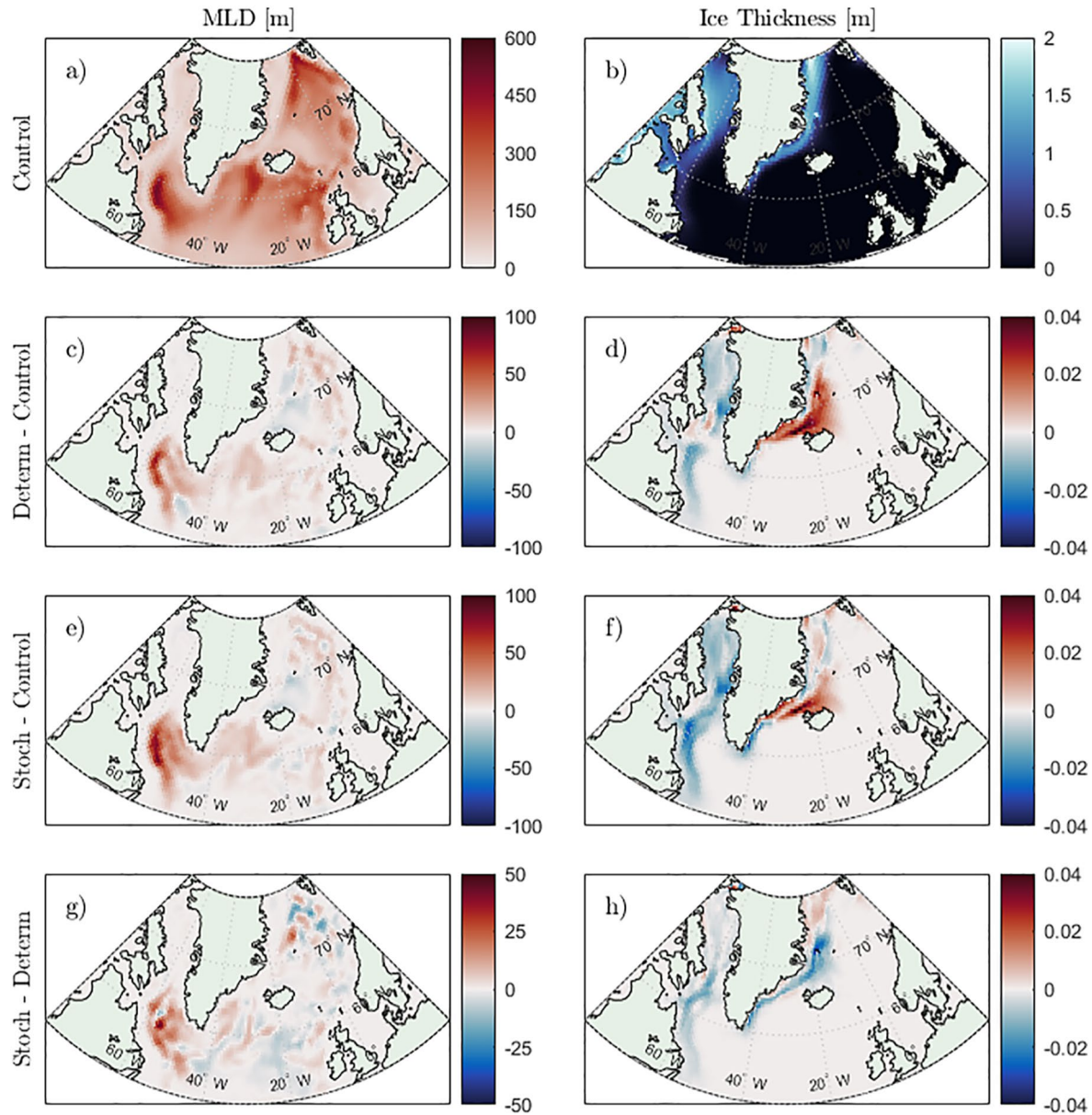


**Figure 5.** (a–b) Control Run 50-year wintertime (JFM) mean state of (a) mixed-layer depths from K-Profile Parameterization, and (b) sea ice thickness. (c–d) Deterministic (PGF) Run minus Control Run of indicated variable. (e–f) Stochastic PGF Run minus Control Run of indicated variable. (g–h) Stochastic PGF Run minus Deterministic PGF Run of indicated variable.

The amplification of the temperature and salinity anomalies in the Labrador Sea is associated with an enhancement of vertical mixing, as indicated by the deepening of wintertime MLDs there (Figures 5c and 5e). In much of the Labrador Sea, the stratification associated with vertical temperature gradients is unstable, that is, the temperature profile generally decreases with depth in the wintertime (Figure S9a in Supporting Information S1, 0–1,000 m) and in the annual mean below ~50 m (not shown). On the other hand, the profile of salinity tends to stabilize the stratification, that is, salinity increases with depth (Figure S9b in Supporting Information S1). In this regime, the stratification is strongly influenced by vertical salinity gradients, and the warm and saline anomaly tends to destabilize the stratification, leading to increased convection depths and the vertical redistribution of the relatively warm, salty water at depth. Associated with the warming of the Labrador Sea, wintertime sea ice cover is reduced near the Labrador Current (Figures 5d and 5f). Conversely, in the Nordic Seas, particularly in the Iceland Sea, cooler surface temperatures lead to a reduction in sea ice melting which manifests as a region of increased sea ice thickness. Consistent with the increase in wintertime convection in the Labrador Sea, the

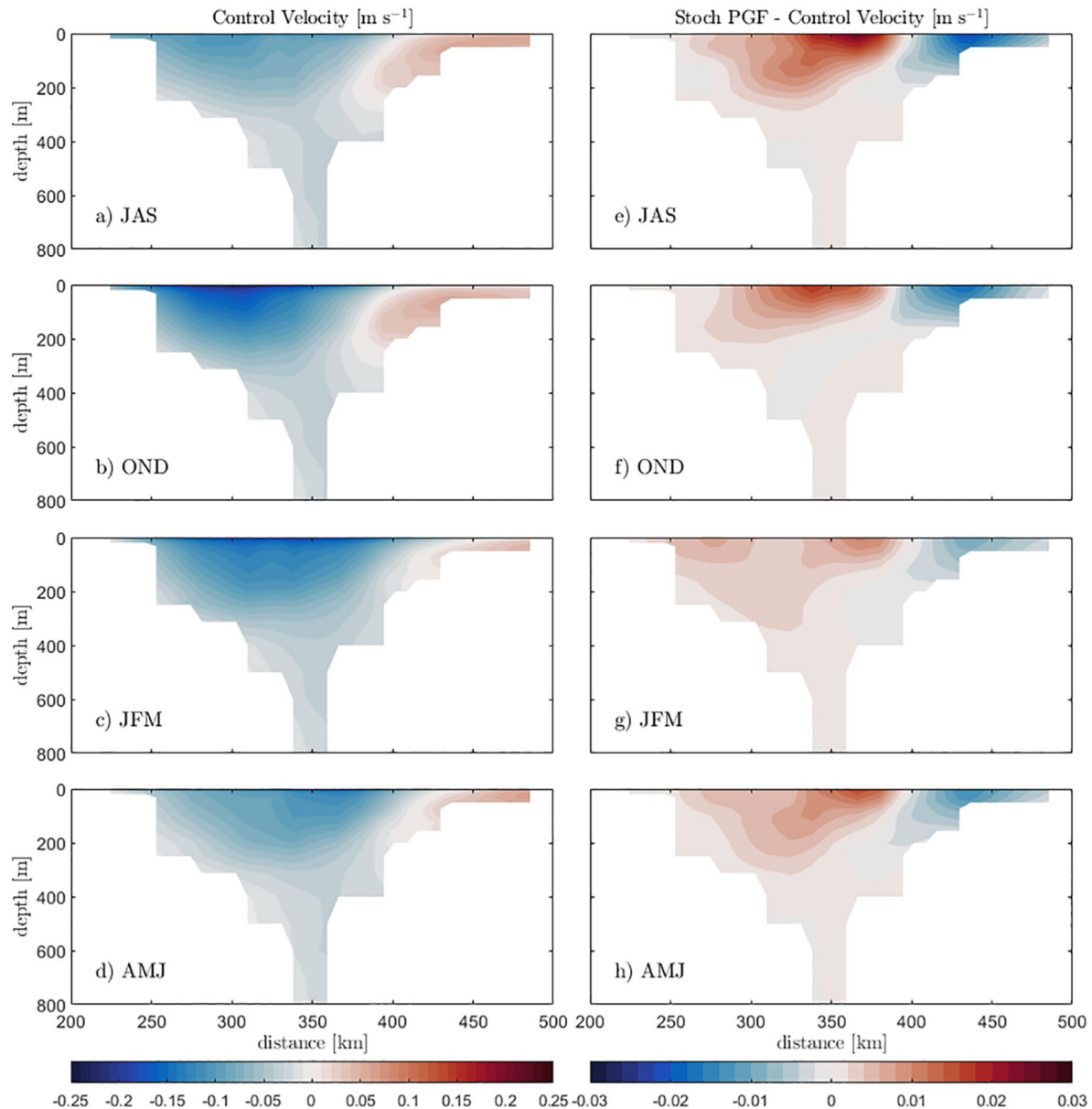


**Figure 6.** (a–d) Control Run velocity through Denmark Strait (i.e., normal to the transect given in Figure 7a) by indicated season. Transect is oriented such that distance increases to the East of Greenland, and positive velocities indicate northeastward flow. (e–h) stochastic pressure gradient force Run minus Control Run of velocity.

maximum of the overturning streamfunction increases by  $\sim 0.3$  Sv in the Deterministic PGF Run and  $\sim 0.4$  Sv in the Stochastic PGF Run, relative to a baseline of  $\sim 14.1$  Sv in the Control Run (Figures S10–S12 in Supporting Information S1).

### 3.3. Gulf Stream Position and Transport

The Gulf Stream, the western boundary current of the subtropical gyre in the North Atlantic Ocean, and the North Atlantic Current, its northward extension, are upper-ocean components of the Atlantic Meridional Overturning Circulation and play a major role in the northward heat transport. In the process of North Atlantic Deep Water formation, the warm waters of the Gulf Stream undergo heat and buoyancy loss associated with strong air-sea heat fluxes in the North Atlantic Ocean. The representation of the Gulf Stream in ocean models thus has implications for the representation of dynamic and thermodynamic processes more broadly. Yet in coarse-resolution

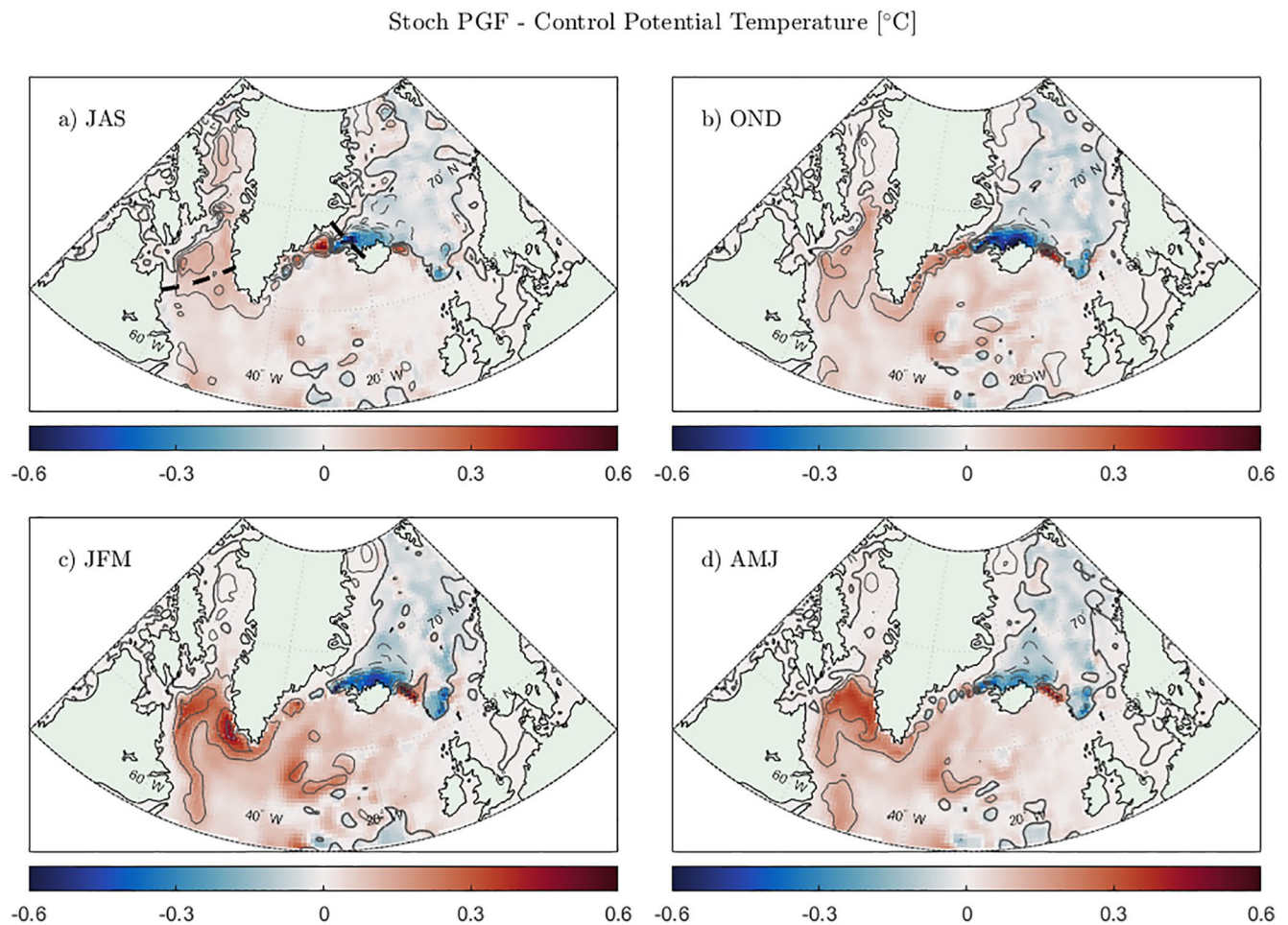


**Figure 7.** (a–d) Stochastic pressure gradient force Run minus Control Run of indicated 50-year seasonal mean of potential temperature (colormap) and salinity (contour lines in increments of 0.03 psu) at 2.5 m. The dashed black line near Denmark Strait in panel a represents the location of the transect in Figure 6, oriented such that distance increases to the East of Greenland. The dashed black line in the Labrador Sea represents the location of the transect in Figure S9 in Supporting Information S1.

ocean models, the separation latitude of the Gulf Stream suffers from a persistent poleward bias which tends to abate as the horizontal grid-cell resolution is refined to that of the first baroclinic mode Rossby radius (e.g., Bryan et al. (2007); Chassignet and Xu (2017)). A wide variety of factors have been proposed to influence the separation latitude of the Gulf Stream in numerical ocean models, including boundary conditions, coastline geometry, topographic effects, subgridscale parameterizations, and others. However, a unifying theory has not yet emerged (Chassignet & Marshall, 2008).

The separated Gulf Stream is associated with the boundary of the North Atlantic (cyclonic) subpolar and (anticyclonic) subtropical gyres (Figure 8a); variability in the separation region is reflected by the strong variance in the SSH field (Figure 8a). A proxy for the Gulf Stream North Wall position (i.e., the  $12^{\circ}\text{C}$  isotherm at 400 m) in the Control Run is compared with that of the gridded EN4 analysis (Good et al., 2013), an observational data product, for the same 50-year period (Figure 9); this comparison suggests that the Control Run has a mean longitudinal bias of  $\sim 0.6^{\circ}$  in the separation region of  $\sim 73^{\circ}\text{--}65^{\circ}\text{W}$ .

In the Gulf Stream region, the SGS temperature variance parameterization and density corrections are highly active (Figures 1a and 1b), resulting in large-scale changes in the regional ocean circulation as indicated by the SSH fields (Figures 8c–8f). The deterministic and stochastic variants of the parameterization give rise to qualitatively similar changes in the circulation (Figures 8c, 8e and 8g). In general, the ocean response in this region is characterized by a strengthening and equatorward shift (Figure 9) of the Gulf Stream. According to geostrophy, the Gulf Stream transport is related to the cross-stream SSH gradient (Figure 8a). The change in the cross-stream



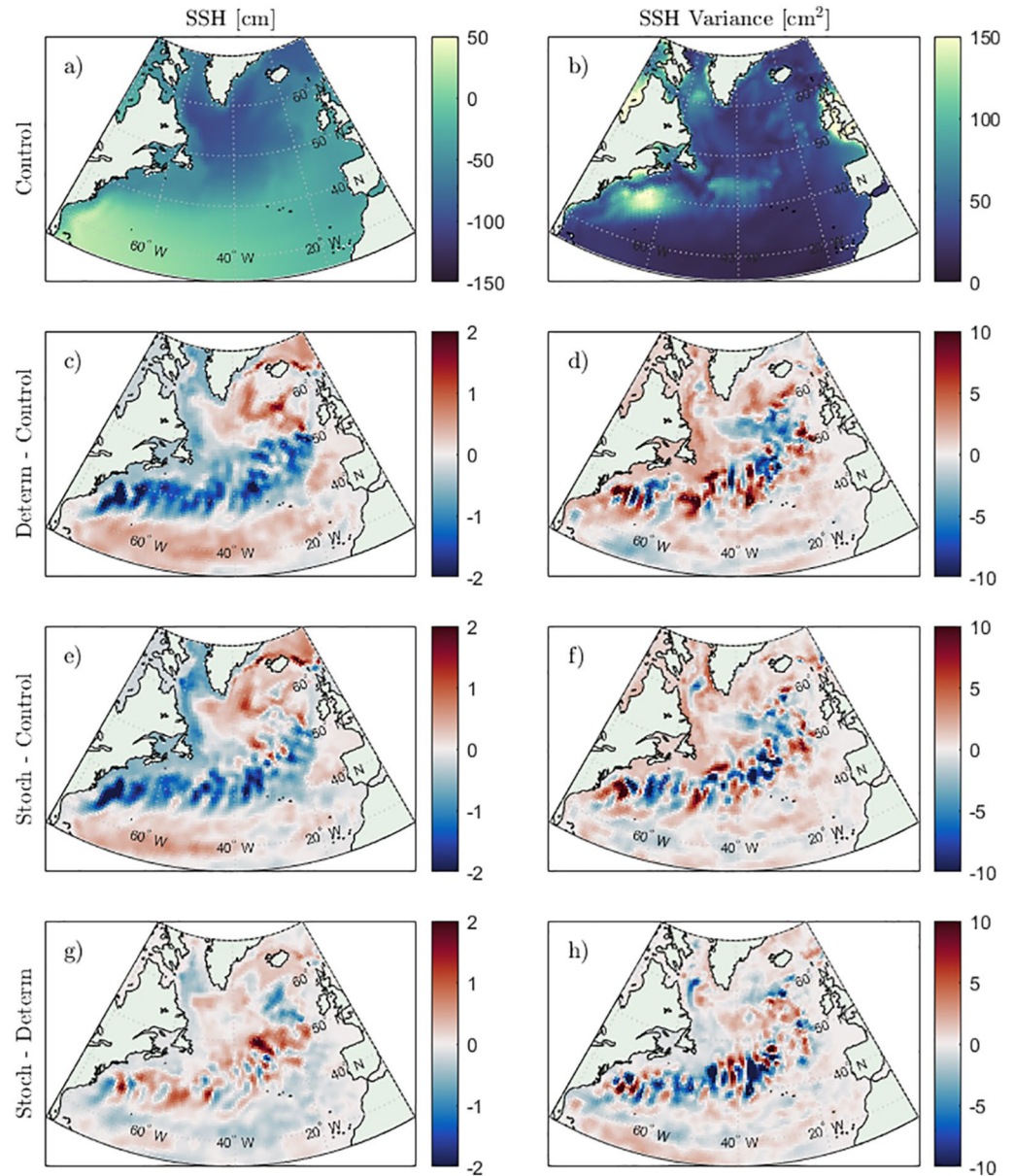


**Figure 8.** (a) Control Run 50-year mean state of sea surface height. (b) Control Run variance, including timescales from 2 hours to 50 years (c–d) Deterministic pressure gradient force (PGF) Run minus Control Run of indicated variable. (e–f) Stochastic PGF Run minus Control Run of indicated variable. (g–h) stochastic PGF Run minus Deterministic PGF Run of indicated variable.

SSH gradient is longitudinally varying and increases by  $\sim 5\%$  in the Experimental Runs relative to the Control Run in the range of  $\sim 65\text{--}55^\circ\text{W}$ . Furthermore, the southward displacement of the Gulf Stream reduces the bias in the Control Run by  $\sim 0.2^\circ$  in the region of  $\sim 73\text{--}65^\circ\text{W}$  relative to the EN4 analysis product.

However, a mechanistic description for the shift of the Gulf Stream remains unclear. Viewing the Gulf Stream as a geostrophically balanced flow, corrections to the meridional PGF along the mean path of the separated current do not directly account for the southward displacement. We explain this using a simplified model in Section S1 in Supporting Information S1 but the direct effect should be to displace the current poleward. It remains uncertain why there is an equatorward shift of the Gulf Stream in the Experimental Runs relative to the Control Run but the response is consistent with prior studies of ocean stochastic parameterizations (Brankart, 2013; Zanna et al., 2019).

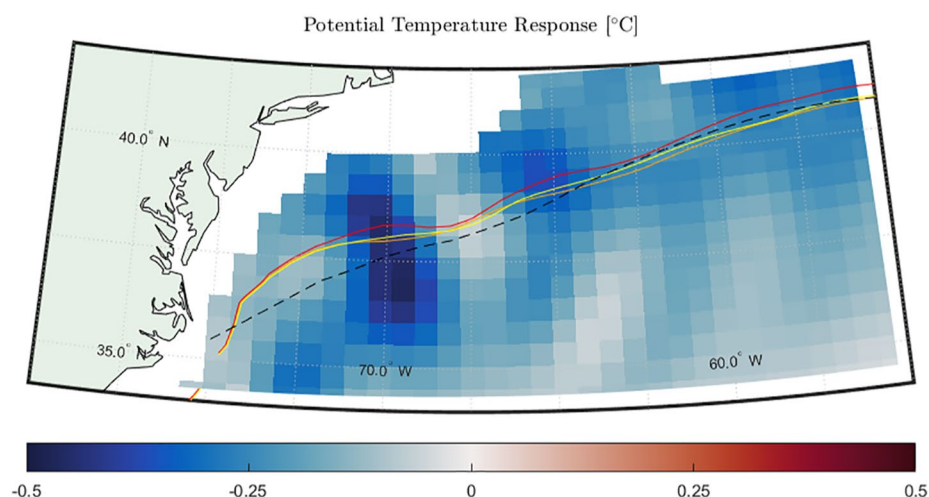


**Figure 9.** Deterministic pressure gradient force (PGF) Run minus Control Run of potential temperature at 400 m (colormap). Red, orange, yellow, and black dashed contours indicate the 12°C isotherm at 400 m in the Control Run, Deterministic PGF Run, and stochastic PGF Run, and EN4 analysis, respectively. Data are 50-year means.

As described in Section 3.1, the SSH variance does not increase considerably in the Experimental Runs relative to the Control Run, globally or in the Gulf Stream region (Figures 8d–8f). In certain regions, the variance is reduced in the Experimental Runs, in some cases more so with the stochastic version of the parameterization, although there is considerable uncertainty as the signal is very noisy (8d,f,h). These differences are likely related to the southward displacement of the mean current, which is associated with a reduction in variability along its prior mean path.

### 3.4. South Atlantic Ocean

The Brazil Current, the western boundary current of the subtropical gyre in the South Atlantic Ocean, transports relatively warm, saline subtropical water poleward, while the Malvinas Current, a branch of the Antarctic Circumpolar Current, transports relatively cold, fresh subantarctic water equatorward. The Brazil-Malvinas Confluence refers to the intersection of these currents off of the eastern coast of South America, which is a region of strong water property gradients. The South Atlantic Current, representing the southern boundary of the subtropical gyre in the South Atlantic Ocean, is fed by the Brazil Current and flows eastward alongside the Antarctic Circumpolar Current to the south. In the Control Run, the South Atlantic Current is characterized by a tongue of relatively warm, salty water (compared with the hydrographic conditions to the north and south) extending eastward across the basin at ~40°S (Figures S17, S18, S19 and S20a–S20d in Supporting Information S1).

Owing to the strong lateral temperature gradients near the Brazil-Malvinas Confluence, the SGS temperature variance parameterization and density corrections are locally elevated (Figures 1a and 1b). In both the Experimental Runs, the Brazil Current extends further south before separating from the coast relative to the Control Run, as evidenced by the dipole pattern of temperature and salinity anomalies near the front (i.e., the positive anomaly of temperature and salinity at ~41°S, ~57°W and the negative anomaly to the northeast at 2.5 m; Figure 10 and 11a–11d). The dipole pattern of temperature and salinity anomalies develops along the coast of South America in summer (JFM), when the Brazil Current/South Atlantic Current is fed by particularly warm subtropical water (Figure 11a). The cold, fresh signal is observed to propagate westward along the prior path of the South Atlantic Current during subsequent seasons and to dissipate by winter (JAS; Figures 11a–11d). (The depth-dependence of the seasonality is characterized in section S2 in Supporting Information S1.) Nevertheless, the ocean response to the deterministic and stochastic parameterizations differs both qualitatively and quantitatively. In the Stochastic PGF Run, the water property dipole is present, with varying amplitude, from the surface to 400 m and below (Figures 11a–11d, S21, S22 and S23a–S23d in Supporting Information S1), while it is considerably weaker in the Deterministic PGF Run (compare Figures 10a–10d and 11a–11d) and is not significantly present at 400 m (not shown). The greater ocean response in the Stochastic PGF Run relative to the Deterministic PGF Run is a rectified effect of the noise.

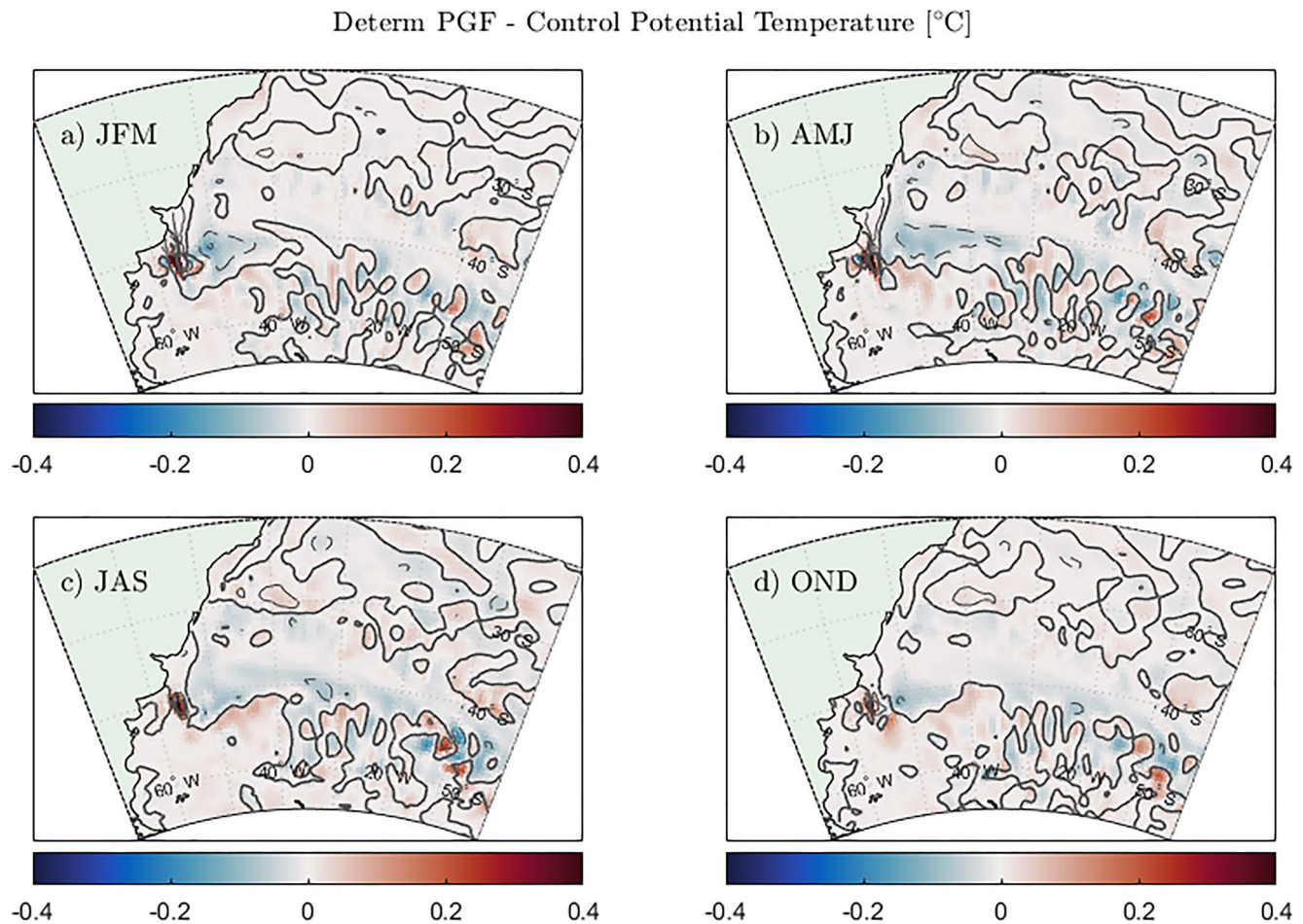


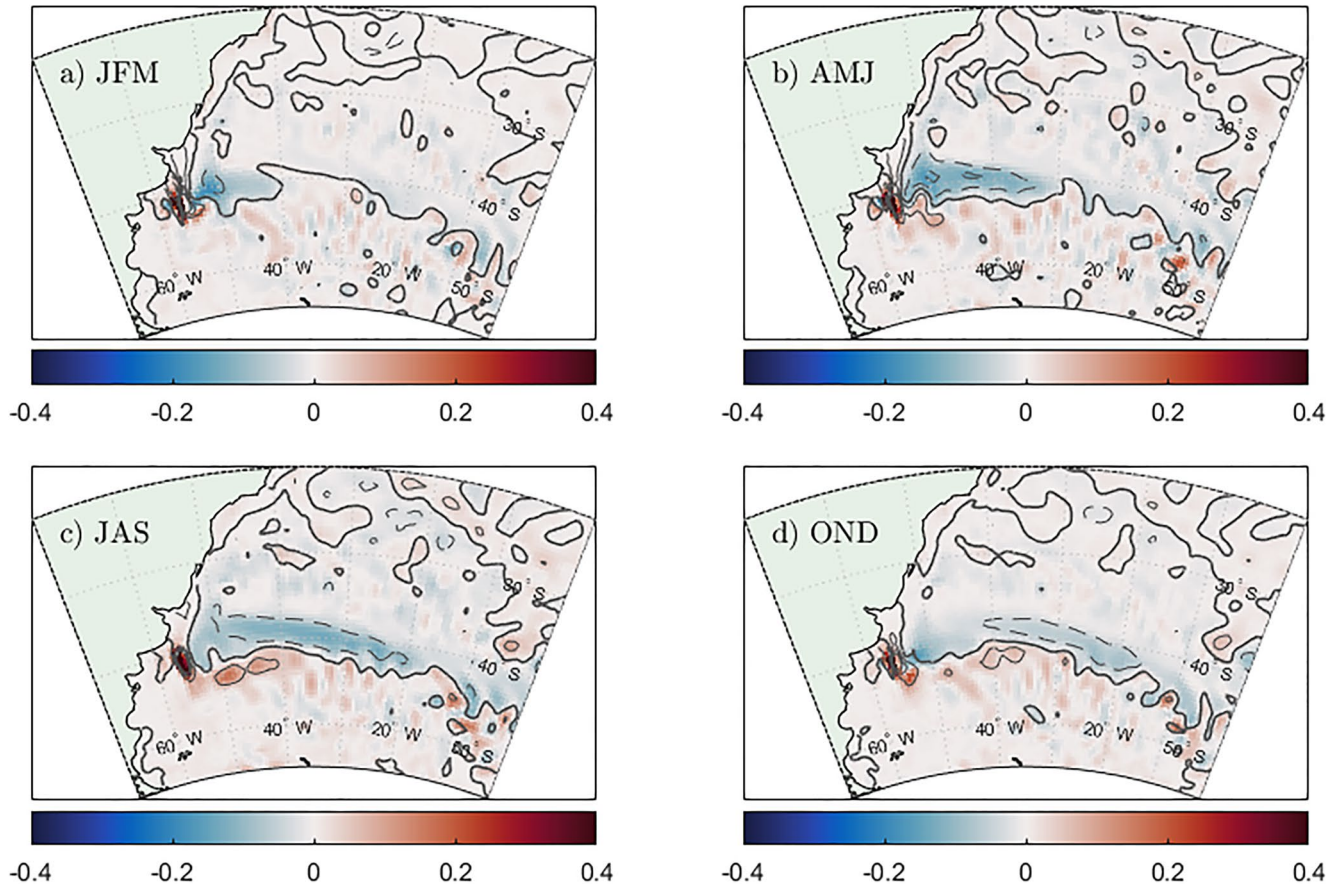
**Figure 10.** (a–d) Deterministic pressure gradient force Run minus Control Run of indicated 50-year seasonal mean of potential temperature (colormap) and salinity (contour lines in increments of 0.02 psu) at 2.5 m.

#### 4. Discussion and Conclusions

Coarse-resolution ocean models contain dynamically significant errors in horizontal density gradients associated with estimating the mean density by applying the nonlinear EOS to the grid-cell-mean temperature and salinity. The SGS temperature variance parameterization of Stanley et al. (2020) was developed to provide an empirically validated and computationally efficient correction to the large-scale density field, but the ocean response to this correction has been hitherto unknown. In this study, we have implemented the deterministic and stochastic versions of this parameterization in the horizontal PGF of CESM-MOM6 and performed hindcast sensitivity experiments to quantify changes in the long-term mean and variability of the ocean state.

In general, the parameterization leads to multifaceted changes in the mean hydrographic conditions and circulation, particularly in the Atlantic Ocean (Figures 2d–2i). In many regions, the changes associated with the deterministic and stochastic parameterizations are qualitatively, if not quantitatively, similar. In the North Atlantic Ocean, cooling and freshening of the Nordic Seas and warming and salinification of the Labrador Sea result (Figures 4c–4f). These changes are primarily attributed to a seasonally varying reduction in the upper-ocean exchange at Denmark Strait in the Experimental Runs relative to the Control Run (Figures 6e–6h), resulting in a dipole pattern of temperature and salinity anomalies which propagates with the mean circulation (Figures 7a–7d). Thus, the upper ocean in the Nordic Seas cools and freshens, while the Labrador Sea warms and salinifies (Figures 4c–4f). The warming of the Labrador Sea is amplified by the intensification of wintertime deep convection which is triggered by the positive salinity anomaly (Figures 5c and 5e). The changes in upper-ocean temperature are associated with the enhanced growth of sea ice in the western Nordic Seas and reduced growth along the Labrador Current (Figures 5d and 5f).



Stoch PGF - Control Potential Temperature [ $^{\circ}\text{C}$ ]


**Figure 11.** Same as Figure 10, but for the stochastic pressure gradient force Run.

Other changes in the position of dynamically important boundary currents result from the SGS temperature variance parameterization. The separated Gulf Stream shifts to the south and strengthens in the Experimental Runs relative to the Control Run, reducing a well-known bias in coarse-resolution ocean models (Figure 9). In the South Atlantic Ocean, the separation of the Brazil Current from the coast shifts to the south, leading to the formation of seasonally propagating hydrographic anomalies near the Brazil-Malvinas Confluence (Figures 11a–11d).

Overall, both the deterministic and stochastic density corrections elicit qualitatively similar ocean responses, although amplitudes are generally greater with the stochastic correction; however, regional exceptions have been noted. The majority of the response is associated with the mean correction, and the rectified effects of the noise play a lesser role, albeit a substantial one in certain regions such as the Brazil-Malvinas Confluence. Furthermore, the stochastic version has additional applications in the context of ensemble generation and data assimilation. Both parameterizations are highly efficient; the cost of computing the deterministic and stochastic parameterizations of SGS temperature variance amounts to  $\sim 1\%$  and  $\sim 2\%$  of the total cost, respectively. In ocean modeling applications, the deterministic version of the parameterization could offer a sufficient approximation of the mean effect of the stochastic parameterization, depending on the target application.

It is a priori unclear to what extent the dynamical response to the Brankart (2013) and Stanley et al. (2020) parameterizations should qualitatively differ, given the theoretical and mathematical differences in their formulations. Nevertheless, certain changes in the ocean mean state, such as the equatorward shift and strengthening of the Gulf Stream, have been reported to result from the Brankart (2013) parameterization in both a coarse-resolution and an eddy-permitting configuration of NEMO (Zanna et al., 2019). Yet the SSH changes in the North Atlantic Ocean associated with the Stanley et al. (2020) parameterization in MOM6 differ somewhat from those associated with

the Brankart (2013) parameterization in NEMO. For instance, both Brankart (2013) and Zanna et al. (2019) have found that the SSH in the Labrador Sea and along the northwestern North Atlantic shelf generally increases in response to their parameterizations, in contrast with our findings (compare Figures 8c and 8e with Figure 4 of Zanna et al. (2019)). However, as demonstrated in Section 3.2, the hydrographic changes in the Labrador Sea are largely attributable to remotely generated anomalies (i.e., changes in the circulation near Denmark Strait which result in the export of a warm and saline anomaly to the Labrador Sea). These mechanisms may be relatively weak or absent in Brankart (2013) and Zanna et al. (2019), since the coarse horizontal resolution of ORCA2 may preclude the resolution of some features of the East Greenland Current and Denmark Strait circulation. Moreover, in the eddy-permitting NEMO experiments of Zanna et al. (2019), the density correction is scaled by a function of latitude which attenuates the parameterization at both low and high latitudes. Differences between the ocean responses to the Brankart (2013) parameterization in ORCA2 and the Stanley et al. (2020) parameterization in MOM6 in the Brazil-Malvinas Confluence region may be attributable in part to differences in resolution and hence representation of boundary currents. The eddy-permitting NEMO configuration was regional, precluding a comparison of our studies in that region.

While this study has assessed the ocean response to a parameterization which corrects errors in the large-scale horizontal PGF, the errors associated with the unresolved SGS temperature variability are not confined to this term. For instance, the GM framework is widely used to parameterize unresolved mesoscale eddy variability as an advective flux of buoyancy which reduces the slope of isopycnals, thus simulating the effects of baroclinicity in extracting available potential energy from the fluid (Gent & McWilliams, 1990). In the GM parameterization, the eddy-induced streamfunction is proportional via an eddy buoyancy diffusivity to the isopycnal slope (i.e., a ratio of lateral and vertical buoyancy gradients), which may contain errors associated with applying the nonlinear EOS to grid-cell-mean quantities. Although stochastic perturbations of eddy buoyancy fluxes have recently been tested in an ocean model (Grooms, 2016; Grooms & Kleiber, 2019), a correction to the buoyancy gradient for the interaction of the unresolved SGS variability with the nonlinear EOS has not. Other potential areas where the density correction may be relevant include the mixed-layer restratification parameterization of Fox-Kemper et al. (2008). Ongoing and future work will investigate the ocean response to applying the Stanley et al. (2020) parameterization to correct the isopycnal slope in the GM and Fox-Kemper et al. (2008) frameworks.

#### Acknowledgments

J. S. Kenigson and I. Grooms were supported by the US NSF under grant OCE 1736708. Z. Stanley was supported by NSF DGE 1650115. F. S. Castruccio was partially supported by the grant NA18OAR4310429 from the National Oceanic and Atmospheric Administration (NOAA), Climate Program Office, Climate Variability and Predictability Program; Modeling Analysis, Predictions, and Projections Program; and the NOAA Global Ocean Monitoring and Observing (GOMO) Program, and by the Department of Energy, Earth and Environmental System Modeling, Regional and Global Model Analysis Program. A. Adcroft was supported by award NA18OAR4320123 from the NOAA, U.S. Department of Commerce. We thank Gustavo Marques (NCAR/Climate & Global Dynamics Lab) for extensive technical support. P. Pegion was supported by the NOAA's Unified Forecast System Research-to-Operations Project (UFS-R2O). Computing resources (Computational & Information Systems Laboratory, 2019) were provided by the Climate Simulation Laboratory at NCAR's Computational and Information Systems Laboratory, sponsored by the National Science Foundation and other agencies.

#### Data Availability Statement

The model data needed to reproduce the figures is located at <https://doi.org/10.5065/wmjm-0r88>. The MOM6 source code can be obtained at <https://doi.org/10.5281/zenodo.5793964>. All model data are stored on the NCAR/CGD storage system.

#### References

- Adcroft, A., Anderson, W., Balaji, V., Blanton, C., Bushuk, M., Dufour, C. O., et al. (2019). The GFDL global ocean and sea ice model OM4.0: Model description and simulation features. *Journal of Advances in Modeling Earth Systems*, 11(10), 3167–3211. <https://doi.org/10.1029/2019ms001726>
- Adcroft, A., & Campin, J.-M. (2004). Rescaled height coordinates for accurate representation of free-surface flows in ocean circulation models. *Ocean Modelling*, 7(3–4), 269–284. <https://doi.org/10.1016/j.ocemod.2003.09.003>
- Bachman, S. D. (2019). The GM+ E closure: A framework for coupling backscatter with the Gent and McWilliams parameterization. *Ocean Modelling*, 136, 85–106. <https://doi.org/10.1016/j.ocemod.2019.02.006>
- Brankart, J.-M. (2013). Impact of uncertainties in the horizontal density gradient upon low resolution global ocean modelling. *Ocean Modelling*, 66, 64–76. <https://doi.org/10.1016/j.ocemod.2013.02.004>
- Bryan, F. O., Hecht, M. W., & Smith, R. D. (2007). Resolution convergence and sensitivity studies with North Atlantic circulation models. Part I: The western boundary current system. *Ocean Modelling*, 16(3–4), 141–159. <https://doi.org/10.1016/j.ocemod.2006.08.005>
- Chassignet, E. P., & Marshall, D. P. (2008). Gulf Stream separation in numerical ocean models. *Geophysical Monograph Series*, (Vol. 177).
- Chassignet, E. P., & Xu, X. (2017). Impact of horizontal resolution (1/12–1/50) on Gulf Stream separation, penetration, and variability. *Journal of Physical Oceanography*, 47(8), 1999–2021. <https://doi.org/10.1175/jpo-d-17-0031.1>
- Computational, & Information Systems Laboratory. (2019). *Cheyenne: HPE/SGI ICE XA system (climate simulation laboratory)*. National Center for Atmospheric Research Boulder. <https://doi.org/10.5065/D6RX99HX>
- Danabasoglu, G., Lamarque, J.-F., Bacmeister, J., Bailey, D., DuVivier, A., & Edwards, J. (2020). The community Earth system model version 2 (CESM2). *Journal of Advances in Modeling Earth Systems*, 12(2). <https://doi.org/10.1029/2019ms001916>
- Fox-Kemper, B., Ferrari, R., & Hallberg, R. (2008). Parameterization of mixed layer eddies. Part I: Theory and diagnosis. *Journal of Physical Oceanography*, 38(6), 1145–1165. <https://doi.org/10.1175/2007jpo3792.1>
- Gent, P. R., & McWilliams, J. C. (1990). Isopycnal mixing in ocean circulation models. *Journal of Physical Oceanography*, 20(1), 150–155. [https://doi.org/10.1175/1520-0485\(1990\)020<0150:imicm>2.0.co;2](https://doi.org/10.1175/1520-0485(1990)020<0150:imicm>2.0.co;2)

- Good, S. A., Martin, M. J., & Rayner, N. A. (2013). EN4: Quality controlled ocean temperature and salinity profiles and monthly objective analyses with uncertainty estimates. *Journal of Geophysical Research*, 118(12), 6704–6716. <https://doi.org/10.1002/2013jc009067>
- Griffies, S. M., Adcroft, A., & Hallberg, R. W. (2020). A primer on the vertical Lagrangian-remap method in ocean models based on finite volume generalized vertical coordinates. *Journal of Advances in Modeling Earth Systems*, 12(10), e2019MS001954. <https://doi.org/10.1029/2019ms001954>
- Griffies, S. M., Danabasoglu, G., Durack, P. J., Adcroft, A. J., Balaji, V., Böning, C. W., et al. (2016). OMIP contribution to CMIP6: Experimental and diagnostic protocol for the physical component of the ocean model intercomparison project. *Geoscientific Model Development*, 9(9), 3231–3296. <https://doi.org/10.5194/gmd-9-3231-2016>
- Grooms, I. (2016). A Gaussian-product stochastic Gent-McWilliams parameterization. *Ocean Modelling*, 106, 27–43. <https://doi.org/10.1016/j.ocemod.2016.09.005>
- Grooms, I., & Kleiber, W. (2019). Diagnosing, modeling, and testing a multiplicative stochastic Gent-McWilliams parameterization. *Ocean Modelling*, 133, 1–10. <https://doi.org/10.1016/j.ocemod.2018.10.009>
- Grooms, I., Lee, Y., & Majda, A. J. (2015). Numerical schemes for stochastic backscatter in the inverse cascade of quasigeostrophic turbulence. *Multiscale Modeling and Simulation*, 13(3), 1001–1021. <https://doi.org/10.1137/140990048>
- Heuzé, C. (2017). North Atlantic deep water formation and AMOC in CMIP5 models. *Ocean Science*, 13(4), 609–622. <https://doi.org/10.5194/os-13-609-2017>
- Hunke, E. C., Lipscomb, W. H., Turner, A. K., Jeffery, N., & Elliott, S. (2010). CICE: The Los Alamos Sea ice model documentation and software user's manual version 5.1 LA-CC-06-012. *T-3 Fluid Dynamics Group Los Alamos National Laboratory* (Vol. 675, p. 500).
- Jansen, M. F., Adcroft, A., Khani, S., & Kong, H. (2019). Toward an energetically consistent, resolution aware parameterization of ocean mesoscale eddies. *Journal of Advances in Modeling Earth Systems*, 11(8), 2844–2860. <https://doi.org/10.1029/2019ms001750>
- Juricke, S., Danilov, S., Koldunov, N., Oliver, M., Sein, D., Sidorenko, D., & Wang, Q. (2020). A kinematic kinetic energy backscatter parameterization: From implementation to global ocean simulations. *Journal of Advances in Modeling Earth Systems*, 12(12), e2020MS002175. <https://doi.org/10.1029/2020ms002175>
- Large, W. G., McWilliams, J. C., & Doney, S. C. (1994). Oceanic vertical mixing: A review and a model with a nonlocal boundary layer parameterization. *Reviews of Geophysics*, 32(4), 363–403. <https://doi.org/10.1029/94rg01872>
- Latarius, K., & Quadfasel, D. (2016). Water mass transformation in the deep basins of the Nordic Seas: Analyses of heat and freshwater budgets. *Deep Sea Research Part I: Oceanographic Research Papers*, 114, 23–42. <https://doi.org/10.1016/j.dsr.2016.04.012>
- Marshall, D. P., Maddison, J. R., & Berloff, P. S. (2012). A framework for parameterizing eddy potential vorticity fluxes. *Journal of Physical Oceanography*, 42(4), 539–557. <https://doi.org/10.1175/jpo-d-11-048.1>
- Stanley, Z., Grooms, I., Kleiber, W., Bachman, S., Castruccio, F., & Adcroft, A. (2020). Parameterizing the impact of unresolved temperature variability on the large-scale density field: Part 1. *Journal of Advances in Modeling Earth Systems*, 12(12), e2020MS002185. <https://doi.org/10.1029/2020ms002185>
- Tsujino, H., Urakawa, S., Nakano, H., Small, R. J., Kim, W. M., Yeager, S. G., et al. (2018). JRA-55 based surface dataset for driving ocean-sea ice models (JRA55-do). *Ocean Modelling*, 130, 79–139. <https://doi.org/10.1016/j.ocemod.2018.07.002>
- White, L., Adcroft, A., & Hallberg, R. (2009). High-order regridding-remapping schemes for continuous isopycnal and generalized coordinates in ocean models. *Journal of Computational Physics*, 228, 8665–8692. <https://doi.org/10.1016/j.jcp.2009.08.016>
- Williams, P. D., Howe, N. J., Gregory, J. M., Smith, R. S., & Joshi, M. M. (2016). Improved climate simulations through a stochastic parameterization of ocean eddies. *Journal of Climate*, 29(24), 8763–8781. <https://doi.org/10.1175/jcli-d-15-0746.1>
- Wright, D. G. (1997). An equation of state for use in ocean models: Eckart's formula revisited. *Journal of Atmospheric and Oceanic Technology*, 14(3), 735–740. [https://doi.org/10.1175/1520-0426\(1997\)014<0735:aeosfu>2.0.co;2](https://doi.org/10.1175/1520-0426(1997)014<0735:aeosfu>2.0.co;2)
- Zanna, L., Brankart, J., Huber, M., Leroux, S., Penduff, T., & Williams, P. (2019). Uncertainty and scale interactions in ocean ensembles: From seasonal forecasts to multidecadal climate predictions. *The Quarterly Journal of the Royal Meteorological Society*, 145, 160–175. <https://doi.org/10.1002/qj.3397>